Mechanical Systems and Signal Processing 242 (2026) 113616

Contents lists available at ScienceDirect

Mechanical Systems and Signal Processing

journal homepage: www.elsevier.com/locate/ymssp

Full Length Article

Enhancing spatial resolution in sparse array ultrasound imaging using nonlinear beamforming: Simulation and experimental validation

Seungo Baek [a], Jinhee Kim [b], Seohee Jeon [b], Hyeong-Ki Kim [c], Choon-Su Park [d,e], Gun Kim [a,*]

[a] School of Civil and Environmental Engineering, Nanyang Technological University, 50 Nanyang Ave, Singapore 639798 Singapore
[b] Department of Civil, Urban, Earth, and Environmental Engineering, Ulsan National Institute of Science and Technology (UNIST), UNIST-gil 50, Ulju-gun, Ulsan 44919, Republic of Korea
[c] Department of Architectural Engineering, Chosun University, 309, Pilmun-daero, Dong-gu, Gwangju 61452, Republic of Korea
[d] Non-destructive Metrology Group, Korea Research Institute of Standards and Science (KRISS), 267, Gajeong-ro, Yuseong-gu, Daejeon 34113, Republic of Korea
[e] Department of Precision Measurement, University of Science and Technology (UST), 217, Gajeong-ro, Yuseong-gu, Daejeon 34113, Republic of Korea

ARTICLE INFO

Communicated by Efren Fernandez-Grande

Keywords:
Ultrasound imaging
Null subtraction imaging
Sparse array
Total focusing method
Nonlinear apodization

ABSTRACT

Sparse array ultrasound imaging offers a cost-effective and scalable solution for nondestructive testing (NDT). However, the reduced number of transceiver elements typically compromises resolution and contrast. To address this limitation, this study proposes a novel nonlinear apodization method, null subtraction imaging (NSI), integrated with the total focusing method (TFM-NSI). This approach effectively suppresses side lobe and grating lobe artifacts, thereby improving lateral resolution and contrast without increasing computational complexity. Numerical simulations and experimental studies on steel samples show that TFM-NSI achieves a 36–96 % improvement in lateral resolution and a 71% reduction in artifacts. Notably, TFM-NSI with an 8-element array achieves image quality comparable to conventional TFM with 64 elements, highlighting its superiority in array utilization. Further experiments on reinforced concrete (RC) slab confirm the potential of TFM-NSI for concrete NDT, enabling accurate measurements of rebar size and embedded defects. These results demonstrate TFM-NSI as a promising tool for advanced NDT applications in various engineering domains.

1. Introductions

Nondestructive testing (NDT) plays a pivotal role in modern engineering by enabling the detection of material degradation and structural anomalies without compromising the integrity of tested components. Among various NDT methodologies, including electromagnetic wave-based techniques [1,2] and X-ray computed tomography (CT) [3], ultrasound-based approaches have gained significant attention due to their nondestructive nature [4,5], adjustable penetration depth [6], and direct correlation with the

* Corresponding author.
E-mail addresses: seungo001@e.ntu.edu.sg (S. Baek), chloe3132@unist.ac.kr (J. Kim), jeonsh@unist.ac.kr (S. Jeon), hyeongki@chosun.ac.kr (H.-K. Kim), choonsu.park@kriss.re.kr (C.-S. Park), gun.kim@ntu.edu.sg (G. Kim).

https://doi.org/10.1016/j.ymssp.2025.113616
Received 27 January 2025; Received in revised form 29 August 2025; Accepted 6 November 2025
Available online 10 November 2025

mechanical properties of materials [7,8]. Ultrasound imaging, in particular, stands out in providing detailed spatial information about internal structures, enabling precise localization of defects and differentiation of closely spaced features [9–11]. These capabilities are indispensable in industrial domains such as in situ manufacturing, biomedical engineering, and civil engineering, where detection precision is critical.

The initial development of ultrasound imaging relied on single-element transducers [12,13]. These systems are straightforward in design and involve simple signal processing, making them relatively easy to implement. Techniques like the synthetic aperture focusing technique (SAFT) [14,15] or RL-deconvolution [16,17] effectively leverage these systems to visualize internal structures, providing valuable insights for engineering applications including defect detection in metallic components [18,19] and rebar localization in concrete structures [20]. However, single-element systems come with inherent limitations, as they require mechanical scanning to cover larger areas, which renders the process slow, labor-intensive, and unsuitable for real-time imaging or applications involving complex geometries [12,13]. To overcome these limitations, array-based ultrasound imaging systems were developed [21–23]. In general, array systems employ multiple transducers arranged in one- or two-dimensional arrays, eliminating the need for mechanical scanning and enhancing both image quality and processing speed. Phased arrays, for example, utilize densely packed transducer elements with spacing (pitch) smaller than half the wavelength ($\lambda/2$) [24]. This configuration facilitates precise beam

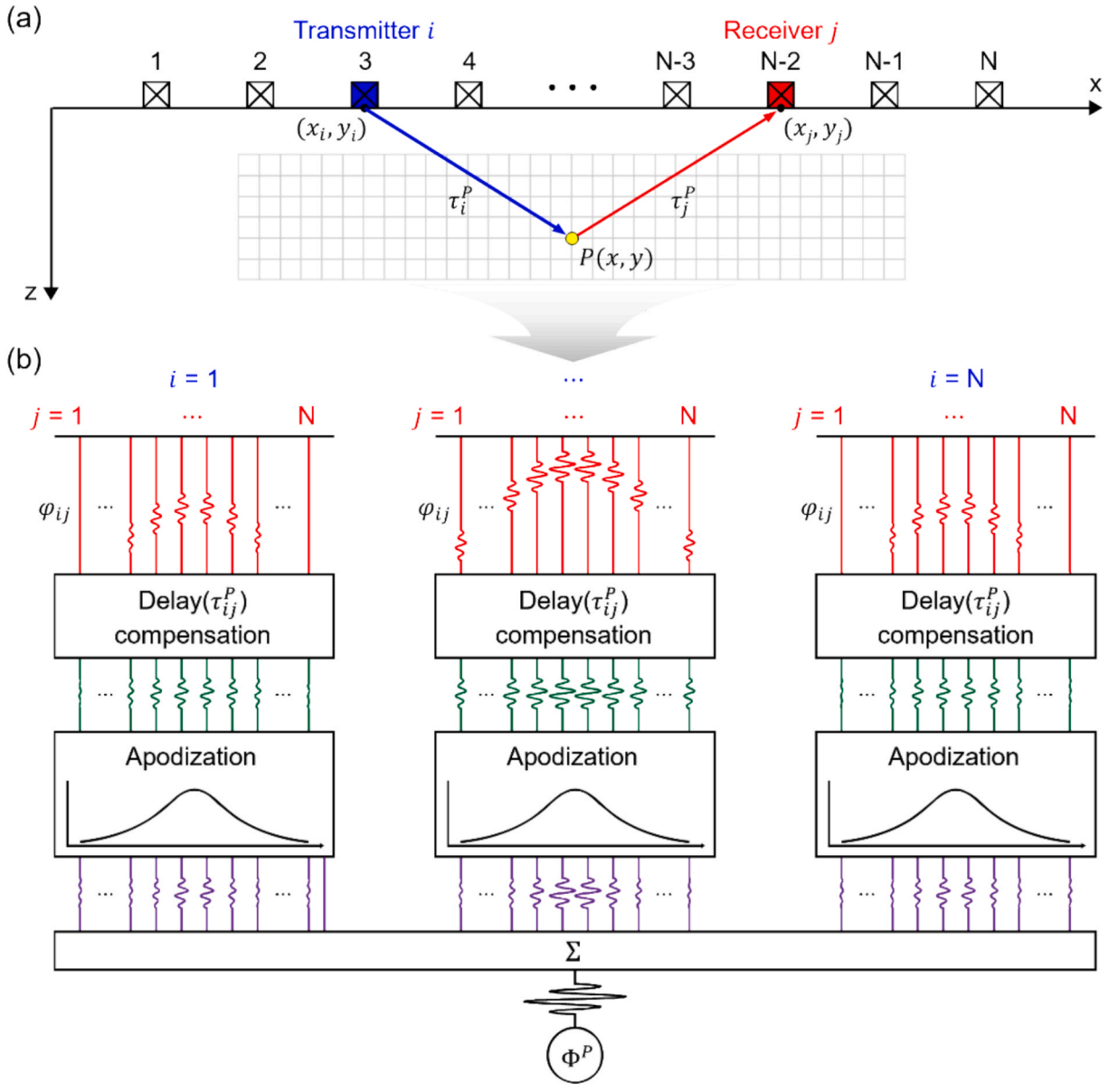

Fig. 1. The principle of TFM with receive apodization: (a) TOF calculation for an arbitrary point reflector; and (b) beam focusing process incorporating the apodization function.

steering and focusing, significantly enhancing sensitivity and accuracy in detecting internal defects [21,25]. Despite these advantages, dense array systems are constrained by expensive hardware costs, increased complexity, and limited scalability, making them impractical for large-scale or cost-sensitive applications.

To tackle these challenges, sparse arrays have emerged as a cost-effective alternative [26–28]. By reducing the number of transducer elements and increasing their spacing, sparse arrays lower hardware costs and computation time while retaining the capability to inspect large areas [29]. However, the increased sparsity compromises the quality and quantity of the acquired ultrasonic signals, resulting in lower resolution, reduced contrast, and increased susceptibility to artifacts. Indeed, this trade-off makes it difficult for users to obtain high-resolution ultrasound images of structures with complex internal features. To overcome these physical constraints, advanced signal acquisition and beamforming techniques, such as full matrix capture (FMC) [30,31] and the total focusing method (TFM) [30,32], have been developed. FMC collects data from all possible transmitter–receiver pairs, providing comprehensive information about internal structures [33]. TFM processes FMC data to reconstruct high-pixel-density images by focusing received beams at every point within the region of interest (ROI), thereby achieving high precision. However, TFM and other beamforming techniques are inherently prone to generating side lobes artifacts [21,34], which distort image features and degrade overall quality. This issue becomes more severe in sparse array configurations, where grating lobes introduces additional image degradation [21].

As one of the latest research trends in ultrasound imaging, researchers have been incorporating advanced signal processing techniques into existing beamforming algorithms to mitigate these persistent challenges. Strategies such as directivity function [35], pairing multiplication [36], and phase coherence factor [37,38] have proven effective in reducing side lobes and artifacts. Building upon these developments, algorithms such as multiple signal classification (MUSIC) [11,39], minimum variance distortionless response (MVDR) [40], and the CLEAN algorithm [41] enable high-resolution, artifact-suppressed imaging, but they demand substantial computational cost and complex processing, often requiring high-performance computing systems. In this context, apodization [42–44] has attracted attention for its simplicity and low computational complexity. By applying predefined weighting functions to shape the radiation pattern of the transducer array, apodization improves image quality without compromising temporal resolution [45]. However, conventional linear apodization methods (e.g., Gaussian or Hann windows) [34,44] achieve side lobe suppression at the expense of broadening the main lobe, which reduces lateral resolution [34].

Recently, nonlinear apodization techniques have shown significant promise in reducing side lobes while enhancing lateral resolution [46–48]. One such method is null subtraction imaging (NSI), which employs three apodization functions and incoherently subtracts the resulting null beams to produce high-resolution images [49–51]. NSI has demonstrated success in biomedical applications, such as *in-vivo* microvessel Doppler imaging [52] and high-contrast ultrasound scanning [53]. However, NSI was originally developed for phased arrays utilizing plane wave imaging (PWI) [49], and its application to sparse arrays remains largely unexplored due to differences in array geometry and wave propagation dynamics. Integrating NSI with sparse arrays thus holds a promising opportunity to address key challenges such as low resolution, poor contrast, and the appearance of side lobe artifacts.

This study investigates the integration of NSI with TFM (TFM-NSI) to improve image quality in sparse array configurations and assess its feasibility for NDT applications. Through numerical simulations and experimental validations using solid engineering materials such as steel blocks and RC structures, the study evaluates the performance of TFM-NSI in comparison with conventional TFM and TFM with linear apodization. The remainder of this paper is structured as follows: Section 2 presents the theoretical framework for integrating NSI with TFM; Section 3 describes numerical simulations conducted on steel structures; Section 4 details experimental validations on steel block and RC structures; and Section 5 summarizes the findings and outlines future work on TFM-NSI for NDT.

2. Beamforming algorithm

2.1. TFM with linear apodization

TFM, a time-domain beamforming technique, reconstructs ultrasound images using the delay-and-sum (DAS) approach [54] applied to acquired radio frequency (RF) signals. Consider an array consisting of N transceiver elements aligned along the x-axis (Fig. 1(a)). In sequential operation, each element operates as a transmitter while all elements simultaneously serve as receivers. This signal acquisition process, known as FMC, stores RF signals from all possible transmit-receive combinations in an $N \times N$ matrix (see Fig. 1(b)). When an ultrasonic pulse is transmitted, a point reflector located at $P(x,y)$ scatters the energy, generating echoes received by all transceiver elements. Let $\varphi_{ij}(t)$ denote the RF signal transmitted by the i-th element at (x_i, y_i) and received by the j-th element at (x_j, y_j). As shown in Fig. 1(a), the time-of-flight (TOF) of the echo, denoted as τ_{ij}^P, is the sum of the travel times of ultrasonic waves from the i-th element to P (τ_i^P) and from P to the j-th element (τ_j^P):

$$\tau_{ij}^P = \tau_i^P + \tau_j^P \tag{1}$$

$$\tau_i^P = \frac{\sqrt{(x_i - x)^2 + (z_i - z)^2}}{c_p} \tag{2}$$

$$\tau_j^P = \frac{\sqrt{(x_j - x)^2 + (z_j - z)^2}}{c_p} \tag{3}$$

where c_p is the longitudinal wave velocity in the material. Once τ_{ij}^P is calculated for all transmitter–receiver pairs, the received beams are focused at P by summing the amplitudes of all φ_{ij}, compensating for their respective τ_{ij}^P values, as described in Fig. 1(b). The amplitude of the beamformed RF signal at P, denoted as Φ^P, is given by:

$$\Phi^P = \sum_{i=1}^{N} \sum_{j=1}^{N} A_j \varphi_{ij}(\tau_{ij}^P) \tag{4}$$

where A_j is the apodization function applied on the receiver side, assigning weights to the summation. To generate a B-mode image, the envelope of the beamformed signals, E_{TFM}, is computed using the Hilbert transform. The obtained E_{TFM} is then log-compressed on a decibel (dB) scale and normalized to the maximum value:

$$E_{TFM,dB} = 20\log_{10}(E_{TFM}) - \max[20\log_{10}(E_{TFM})] \tag{5}$$

The far-field beam pattern generated by an array is determined by the Fourier transform of the product of the aperture and apodization functions [34]. For instance, a rectangular apodization (RCT), represented by the black solid line in Fig. 2(a), produces a sinc function beam pattern, as shown by the black solid line in Fig. 2(b). Linear apodization [43], a mathematical weighting function that maintains a constant phase across all array elements, is commonly adopted to suppress side lobe-induced artifacts. Examples of widely used linear apodization methods include the Hann and Blackman functions, which apply smooth weighting to the aperture. For instance, the Hann function, depicted by the blue dotted line in Fig. 2(a), achieves a significantly higher main-lobe-to-side-lobe ratio, as indicated by the blue dotted line in Fig. 2(b). Fig. 2(e) presents simulated single-point target images reconstructed using both TFM

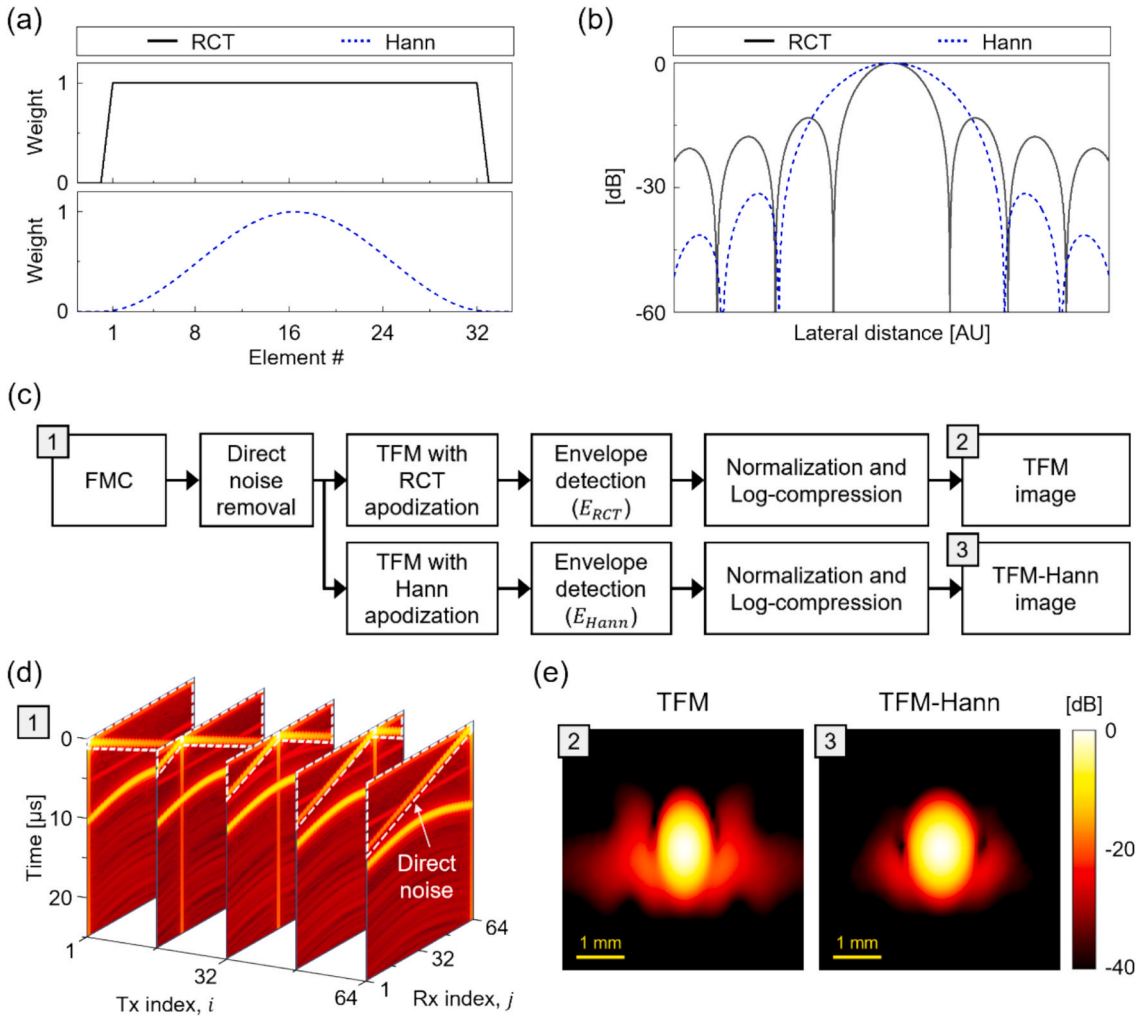

Fig. 2. Linear apodization methods: (a) RCT and Hann apodization functions; (b) their corresponding beam patterns; (c) flowchart of the TFM beamforming process with linear apodization; (d) simulated FMC data for a single point target; and (e) reconstructed B-mode images using RCT and Hann apodizations.

with RCT (TFM) and TFM with Hann apodization (TFM-Hann). The results show that TFM-Hann substantially reduces side lobe artifacts adjacent to the point target owing to the improved main-lobe-to-side-lobe ratio. However, this enhancement inevitably broadens the main lobe beamwidth, leading to a slight reduction in lateral resolution, as evidenced in Fig. 2(b).

2.2. TFM with nonlinear apodization: TFM-NSI

NSI is a nonlinear apodization technique constructed using three different functions: zero-mean (ZM) and two DC-biased functions (DC1 and DC2) [49]. As illustrated in Fig. 3(a), these functions are defined as follows:

$$A_j^{ZM} = \begin{cases} 1 : 1 \le j < \dfrac{N}{2} \\ -1 : \dfrac{N}{2} \le j < N \end{cases} \tag{6}$$

$$A_j^{DC1} = A_j^{ZM} + DC \tag{7}$$

$$A_j^{DC2} = -A_j^{ZM} + DC \tag{8}$$

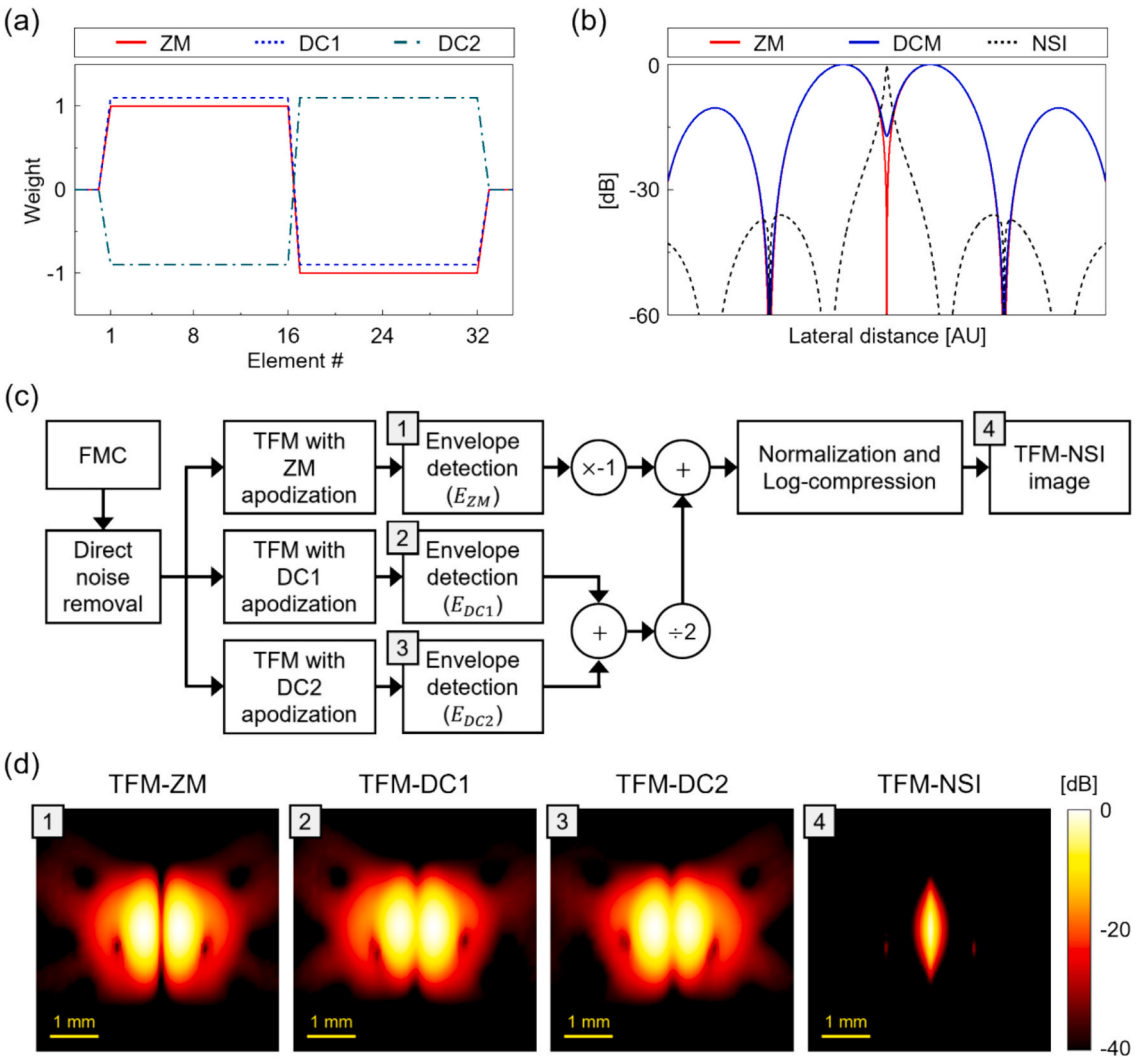

Fig. 3. Nonlinear apodization method: (a) three apodization functions (ZM, DC1, and DC2); (b) their corresponding null beam patterns; (c) flowchart of the TFM-NSI beamforming process; and (d) reconstructed B-mode images obtained using ZM, DC1, and DC2 apodizations, with the final TFM-NSI image.

where *DC* refers to the direct current constant. The ZM apodization, represented by the red solid line in Fig. 3(a), produces a beam pattern characterized by two main lobes and a central null, as shown by the red solid line in Fig. 3(b). For the two DC-biased apodizations, their respective beams are averaged to form the DC-mean (DCM) beam (blue solid line in Fig. 3(b)), which closely resembles the ZM beam, the only difference being a slight positive offset at the null. The NSI beam is then derived by subtracting the ZM beam from the DCM beam. The incoherent compounding of three different null beams makes the NSI beam nonlinear, resulting in a narrow main lobe with a significantly improved main-lobe-to-side-lobe ratio, as illustrated by the black dotted line in Fig. 3(b).

For the TFM beamformer, NSI is integrated by applying the three apodization functions (ZM, DC1, and DC2) during the beam focusing step (Eq. (4)). For each apodization function, the beamformed RF signals are processed to compute their envelopes (E_{ZM}, E_{DC1}, and E_{DC2}) using the Hilbert transform. The TFM-NSI envelope image ($E_{TFM-NSI}$) is then obtained through incoherent subtraction of E_{ZM} from E_{DCM} (Fig. 3(c)):

$$E_{DCM} = \frac{E_{DC1} + E_{DC2}}{2} \tag{9}$$

$$E_{TFM-NSI} = E_{DCM} - E_{ZM} \tag{10}$$

Finally, the TFM-NSI image is generated by converting the $E_{TFM-NSI}$ envelope into a dB scale via log-compression, with the maximum value normalized to zero:

$$E_{TFM-NSI,dB} = 20\log_{10}(E_{TFM-NSI}) - \max[20\log_{10}(E_{TFM-NSI})] \tag{11}$$

Fig. 3(d) shows single-point target images reconstructed using each apodization method, together with the final TFM-NSI result.

Figs. 4(a) and 4(b) present four ZM apodization functions – rectangular (ZM_{RCT}), sine (ZM_{SIN}), triangular (ZM_{TRI}), and polynomial (ZM_{POLY}) – along with their corresponding NSI beam patterns. Among these configurations, the NSI beamformer using the ZM_{RCT} function (NSI_{RCT}) achieves the lowest side lobe level of −30.5 dB, outperforming the NSI_{SIN} (−30.1 dB), NSI_{TRI} (−26.6 dB), and ZM_{POLY} (−18.9 dB). Fig. 4(c) further illustrates the normalized full width at half maximum (FWHM) of the main lobe for each ZM function. The NSI_{RCT} exhibits the narrowest FWHM, highlighting its superior lateral resolution compared to other configurations. The combination of the lowest side lobe level and the narrowest FWHM demonstrates ZM_{RCT} as the optimal ZM function for achieving enhanced imaging performance in null subtraction.

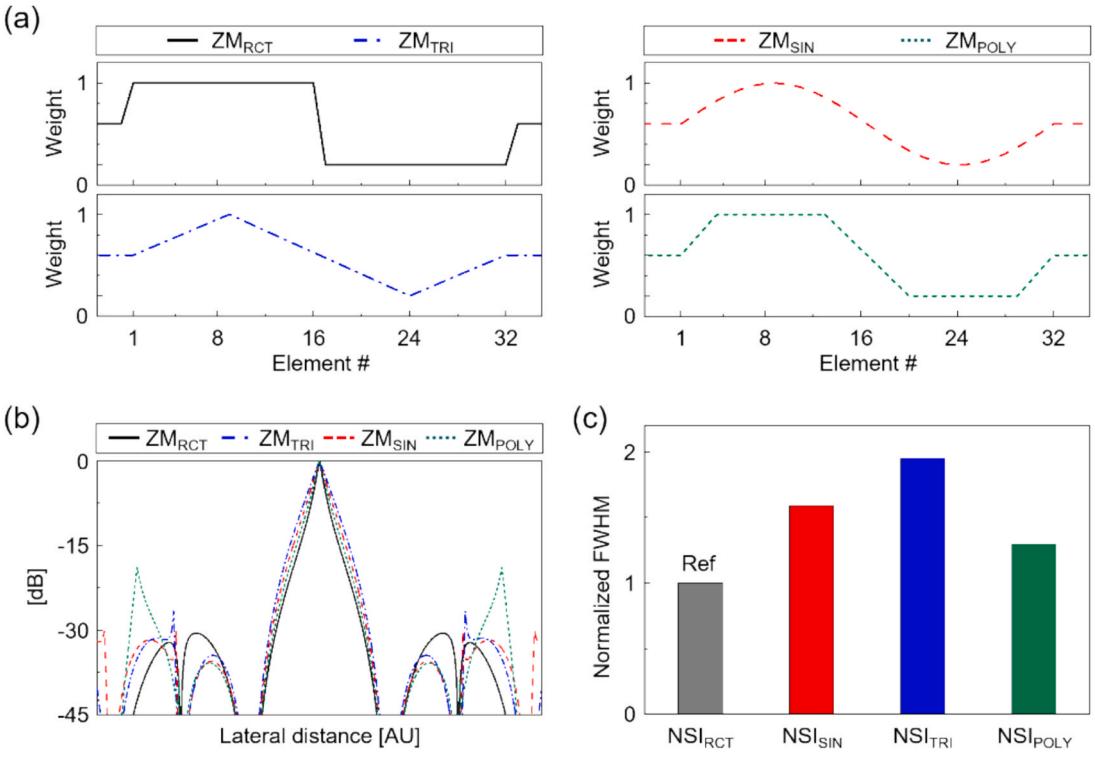

Fig. 4. NSI beam patterns with four different ZM functions: (a) ZM_{RCT}, ZM_{SIN}, ZM_{TRI}, and ZM_{POLY}; (b) their corresponding NSI beam patterns; and (c) normalized FWHM of the main lobe for each NSI beam.

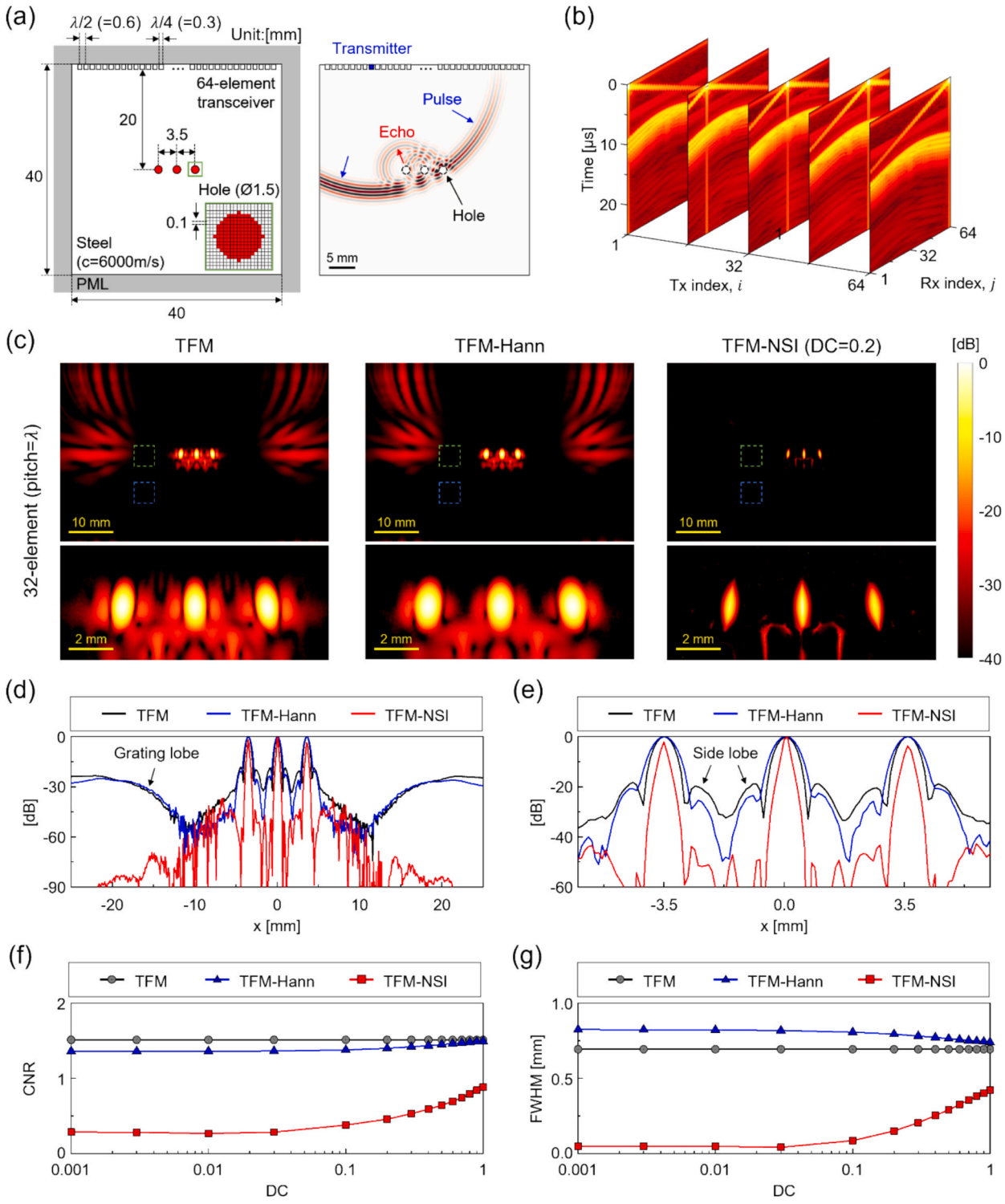

Fig. 5. Numerical simulation for a steel structure: (a) mesh structure and FMC simulation setup; (b) simulated FMC data; (c) reconstructed images using TFM, TFM-Hann, and TFM-NSI beamformers (DC = 0.2), with green and blue boxes indicating the ROI and background noise regions for CNR calculation; (d) lateral cross-sectional images of the three holes; (e) magnified lateral cross-sectional profiles; (f) CNR as a function of the DC constant; and (g) FWHM as a function of the DC constant.

3. Simulations

3.1. Simulation setup for FMC in a steel structure

A numerical simulation of FMC was conducted using the k-Wave MATLAB toolbox [55,56] to evaluate the effectiveness of the proposed method. The simulation domain was configured with dimensions of $40 \times 40 \times 10$ mm^3, and a voxel resolution of 0.1 mm. A steel sample was chosen as the background medium, with material properties assigned as density (ρ) of 7,850 kg/m^3, longitudinal wave velocity (c_p) of 6,000 m/s, and attenuation coefficient (α) of 0.2 dB/MHz/cm. Three lateral hole-shaped reflectors, used as imaging targets, were placed at the center of the sample. These reflectors, with properties of $\rho = 25$ kg/m^3, $c_p = 340$ m/s, $\alpha = 0.2$ dB/MHz/cm, are illustrated in Fig. 5(a).

FMC was executed at an excitation frequency of 5 MHz using a 64-element phased array with a pitch of $\lambda/2$ (= 0.6 mm). The received echo signals were sampled at 200 MHz over a 30 μs duration, producing a simulated FMC dataset stored as a 3D matrix. Fig. 5 (b) shows examples of five representative slice images corresponding to transmitting elements 1, 16, 32, 48, and 64. For image reconstruction, three beamformers were applied to the FMC data: TFM, TFM-Hann, and TFM-NSI. During beamforming, sub-aperture configurations using 64, 32, 16, and 8 uniformly spaced elements were tested, with pitches of $\lambda/2$, λ, 2 λ, and 4 λ, respectively, to simulate sparse array images while preserving the overall aperture size. The performance of each beamformer was quantitatively evaluated based on five criteria: the contrast-to-noise ratio (CNR) of the artifacts, FWHM of the center hole, the signal-to-noise ratio (SNR), the array performance index (API), and the computation time of the image reconstruction process. Note that the CNR was calculated as follows:

$$CNR = \frac{|\mu_{ROI} - \mu_{BGN}|}{\sqrt{\sigma_{ROI}^2 - \sigma_{BGN}^2}} \tag{12}$$

where μ_{ROI} and μ_{BGN} represent the mean envelope intensities of the ROI and the background noise, respectively, while σ_{ROI}^2 and σ_{BGN}^2 denote their respective variances. To evaluate SNR, white Gaussian noise at levels of 10 dB was added to the pre-beamformed RF signals, and the SNR after beamforming was computed as:

$$SNR = 10\log\left(\frac{\mu_{CH}}{\mu_{BGN}}\right) \tag{13}$$

where μ_{CH} represents the mean envelope intensity of center hole. The API was defined as the −6 dB focal area of the center hole normalized by the square of the wavelength ($\lambda^2 = 1.44$ mm^2). For computation time measurements, image reconstruction was repeated 10 times with the same dataset, and the average value was obtained to account for variability in the computing system.

3.2. Performance evaluation of beamformers

Fig. 5(c) presents reconstructed images produced by each beamformer for a 32-element array (pitch = λ), displayed within a −40 dB dynamic range, while Figs. 5(d) and 5(e) provide the corresponding lateral cross-sections of the three holes. The TFM beamformer produces high pixel-density images, successfully detecting all three lateral holes. However, significant artifacts are evident in Fig. 5(c). Specifically, side lobe artifacts appear adjacent to each hole at −18.9 dB, and grating lobe artifacts emerge farther from the holes on either side at –23.3 dB. These artifacts obscure important details on defects, making it difficult to identify smaller or closely spaced flaws.

In contrast, the TFM-Hann beamformer effectively reduces these artifacts, mitigating side lobe and grating lobe levels to −26.8 dB and −25.2 dB, respectively. This improvement is achieved by increasing the main lobe-to-sidelobe ratio through linear apodization, which emphasizes signals received by central elements (see Section 2.2). However, this enhancement leads to a trade-off in lateral resolution, as evidenced by a broader FWHM of 0.83 mm, compared to 0.68 mm with TFM. Among the evaluated methods, the TFM-NSI beamformer demonstrates the most pronounced performance, producing well-focused images of defects while significantly reducing side lobe and grating lobe artifacts to −43.3 dB and −40.9 dB, respectively. Furthermore, TFM-NSI achieves an FWHM of 0.24 mm, representing a 64 % improvement in lateral resolution over conventional TFM. To further examine improvements in lateral resolution, additional simulations are conducted with two closely spaced holes (0.75 λ and 0.25 λ). The results show that TFM-NSI successfully distinguishes the holes even at a spacing of 0.25 λ, whereas TFM resolves them at 0.75 λ but fails at 0.25 λ. A detailed description is provided in Appendix A.

Figs. 5(f) and 5(g) illustrate the effect of varying the DC constant (from 1 to 0.001) on the CNR of grating lobe artifacts and the FWHM of the center hole. For TFM, where equal element weighting is applied, the CNR and FWHM values remain unchanged regardless of the DC constant. TFM-Hann shows a converging trend with TFM results as the DC constant increases because Hann apodization approximates a rectangular function at high DC values. For TFM-NSI, reducing the DC constant from 1 to 0.03 results in a noticeable drop in both CNR and FWHM. Further reductions below 0.03 yield minimal additional effects, as the null bridge in the DCM beam becomes steeper at lower DC values, thereby sharpening the main lobe and suppressing side lobes more effectively. Across all DC values, TFM-NSI consistently achieves lower CNR and FWHM compared to other beamforming methods, with maximum reductions of 82 % and 94 %, respectively. These results clearly show the superior capability of TFM-NSI for high-resolution, high-contrast imaging with robust artifact suppression.

3.3. Effect of array sparsity

Fig. 6(a) presents reconstructed images generated by each beamformer under varying levels of array sparsity. Figs. 6(b) and 6(c) show the CNR and FWHM metrics for DC constants ranging from 1 to 0.001 at different levels of array sparsity. These multivariable evaluations demonstrate the importance of selecting an appropriate DC constant for maintaining image quality when the number of elements is reduced. In general, as the number of elements decreases, side lobe and grating lobe artifacts become more prominent,

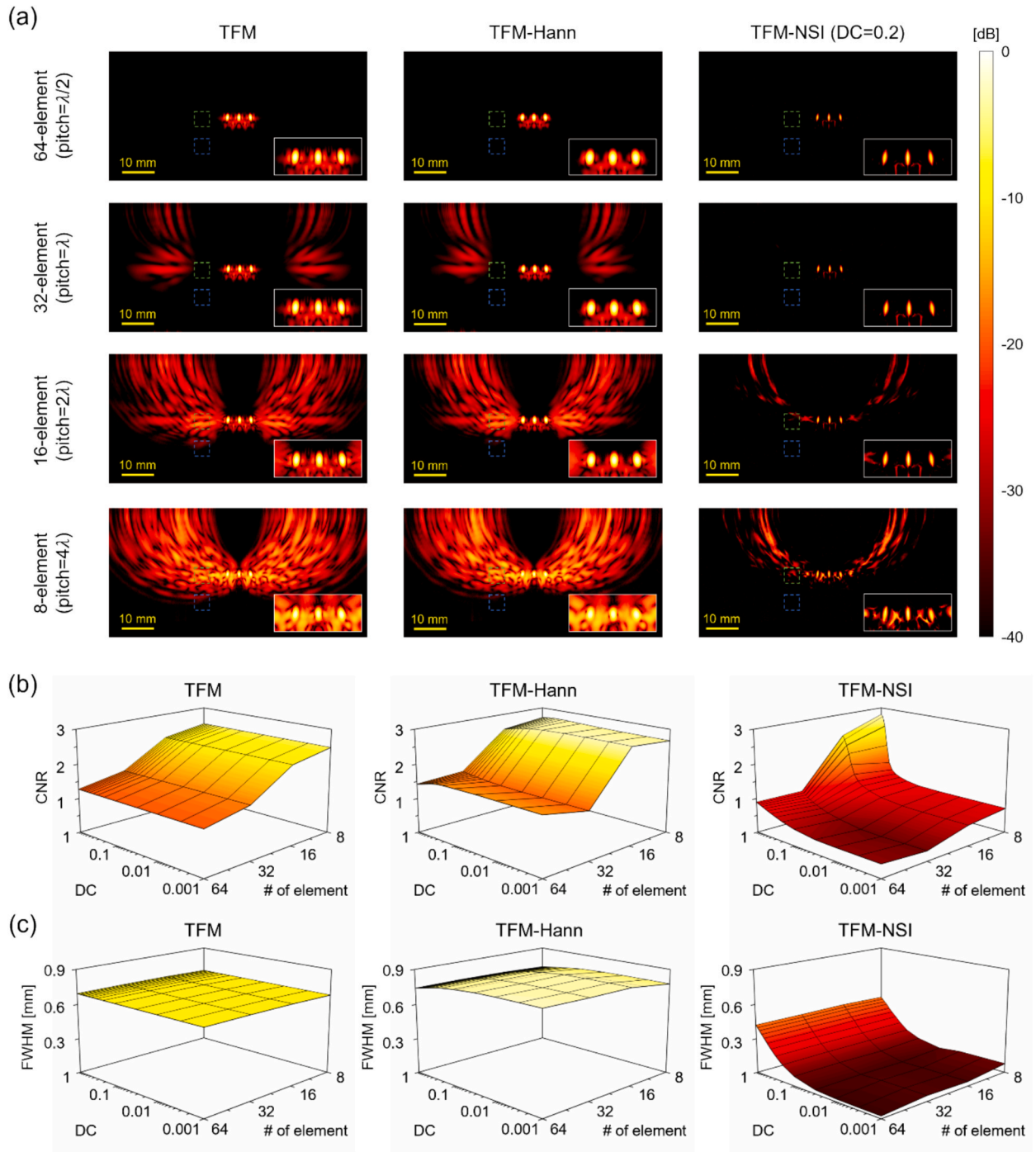

Fig. 6. Effect of array sparsity: (a) reconstructed images using TFM, TFM-Hann, and TFM-NSI with varying levels of array sparsity. The green and blue boxes indicate the ROI and background noise regions used for CNR measurement; (b) CNR matrix as a function of the number of elements and the DC constant; and (c) FWHM matrix as a function of the number of elements and the DC constant.

degrading image quality. For example, CNR values for TFM and TFM-Hann increase dramatically from 1.27 and 1.63 (64 elements) to 2.48 and 2.67 (8 elements), representing 95 % and 64 % deterioration, respectively. For TFM-NSI, the DC constant plays a pivotal role in determining CNR performance relative to array sparsity. With 64 and 32 elements, TFM-NSI consistently achieves lower CNR values than TFM across all DC constants. However, as the array becomes sparser (16 and 8 elements), performance becomes highly dependent on the DC constant. At higher DC values (e.g., DC = 1), TFM-NSI yields a CNR of 2.78, which is even worse than that of TFM. In contrast, at lower DC values (DC < 0.5), TFM-NSI achieves lower CNR values, with a minimum of 0.71 – a 71 % improvement compared with TFM. Furthermore, even with only 8 elements, TFM-NSI achieves a 44 % improvement over TFM with 64 elements. For FWHM, TFM-NSI consistently achieves narrower widths than the other beamformers, as shown in Fig. 6(c). Array sparsity has a minimal impact on lateral resolution, since all beamformers exhibit only slight increases in FWHM with reduced element counts, resulting in a maximum variation of 6 %. The DC constant consistently affects TFM-NSI, with lower values leading to narrower FWHM. The estimated range of FWHM is 0.42–0.02 mm, confirming a 38–96 % improvement over the TFM value of 0.68 mm.

Table 1 summarizes the estimated SNR and API values for each method. For SNR with a fixed DC value of 0.2, TFM-NSI consistently achieves higher values. For example, in the 8-element configuration, both TFM and TFM-Hann yield SNR values of approximately 11 dB, which is close to the 10 dB noise level introduced into the pre-beamformed data. In contrast, TFM-NSI attains an SNR of 18 dB, indicating effective noise suppression. The API analysis shows that TFM and TFM-Hann consistently yield values above 0.4, whereas TFM-NSI remains below 0.1. These results indicate that TFM-NSI produces well-focused defect images compared with the two conventional beamformers. Similar to FWHM, the effect of array sparsity on API is minimal, with maximum variations of only 0.03.

In summary, TFM-NSI demonstrates outstanding performance in maintaining high-resolution and suppressing artifacts, particularly in sparse array configurations, when the DC constant is carefully controlled. The strong dependency on the DC constant under sparse conditions can be attributed to the reduction in total energy available for beamforming. It is generally accepted that the overall transmitted and received energy diminishes as the number of active elements decreases. Consequently, the relative weighting introduced by the DC constant exerts a greater influence on the beam pattern, in proportion to the reduced energy. This observation suggests that tuning the DC constant for different array geometries is essential to achieve consistent image quality. Table 2 summarizes the mean and standard deviation of computation times for each beamformer, measured over 10 repetitions. Since apodization can be implemented using predefined functions, TFM-NSI achieves computation times nearly identical to those of conventional TFM and TFM-Hann. Combined with its improved lateral resolution, these results confirm the computational efficiency of TFM-NSI in enhancing image quality.

4. Experimental validation

4.1. Steel structure with three holes

To experimentally validate the effectiveness of the proposed NSI technique, an ASTM A36 steel sample (Trienco Inc.) with dimensions of 76.5 × 152.0 × 25.5 mm^3 and a longitudinal wave velocity (c_p) of 5,940 m/s was prepared. Fig. 7(a) shows the ROI for image reconstruction, covering 37.5 × 75 mm^2. Within the ROI, three cylindrical side holes, each with a diameter of 1.5 mm, were drilled along the y-axis. Their relative positions are illustrated in Fig. 7(b). FMC data acquisition was performed using a phased array transducer (L7-4, ATL/Philips; center frequency: 5.2 MHz; 128 elements; pitch: 0.295 mm) connected to a Verasonics phased array system (Vantage 64, Verasonics Inc.), as depicted in Figs. 7(c) and 7(d). To ensure proper vertical alignment between the imaging section and the sample surface, the transducer was coupled to the sample using ultrasonic transmission gel (Sanipia, South Korea). Since the transducer pitch (0.295 mm) was smaller than half the wavelength (~0.57 mm), alternative elements of the 128-element array were selectively activated. This configuration resulted in 64 active elements with an effective pitch of 0.59 mm during FMC acquisition. The collected FMC data were subsequently beamformed to generate images using TFM, TFM-Hann, and TFM-NSI. Sub-apertures were configured with the simulation setup (64, 32, 16, and 8 uniformly spaced elements with pitches set to $\lambda/2$, λ, 2 λ, and 4 λ, respectively) to evaluate the effect of array sparsity on the performance of each beamformer.

Fig. 8(a) displays the reconstructed images obtained by each beamformer under varying levels of array sparsity. Figs. 8(b) and 8(c) present the corresponding CNR and FWHM metrics for each beamformer. Consistent with the simulation results, artifacts become more pronounced as the number of elements decreases. However, the experimental results exhibit more severe image degradation, primarily due to speckle noise caused by the grain structure of the steel specimen. For TFM and TFM-Hann, the CNR values at 64 elements are 0.31 and 0.36, respectively. As the number of elements decreases to 8, both beamformers show dramatic increases in CNR, reaching 1.88 and 1.99, which indicates a significant rise in artifact interference. In contrast, TFM-NSI consistently achieves lower CNR values than the other beamformers for all array configurations. Remarkably, with 8 elements, TFM-NSI achieves CNR values ranging from

Table 1
SNR and API values of each beamformer. A 10 dB white Gaussian noise was applied to the pre-beamformed data for SNR evaluation.

Number of elements	SNR [dB]			API		
	TFM	TFM-Hann	TFM-NSI (DC = 0.2)	TFM	TFM-Hann	TFM-NSI (DC = 0.2)
64	25.85	26.17	42.58	0.40	0.45	0.07
32	16.28	16.96	21.61	0.40	0.45	0.08
16	14.15	14.66	18.31	0.41	0.46	0.10
8	11.64	11.84	18.19	0.41	0.46	0.10

Table 2
Computation time for image reconstruction using different beamformers.

Number of elements	Computation time [s]		
	TFM	TFM-Hann	TFM-NSI
64	90.69 (± 0.40)	90.7 (± 0.53)	90.74 (± 0.63)
32	17.25 (± 0.18)	17.28 (± 0.32)	17.30 (± 0.47)
16	5.58 (± 0.22)	5.58 (± 0.42)	5.61 (± 0.25)
8	2.47 (± 0.12)	2.45 (± 0.20)	2.49 (± 0.33)

Note: All computations were conducted using MATLAB R2024a on portable laptop (Apple Silicon M1 Pro CPU).

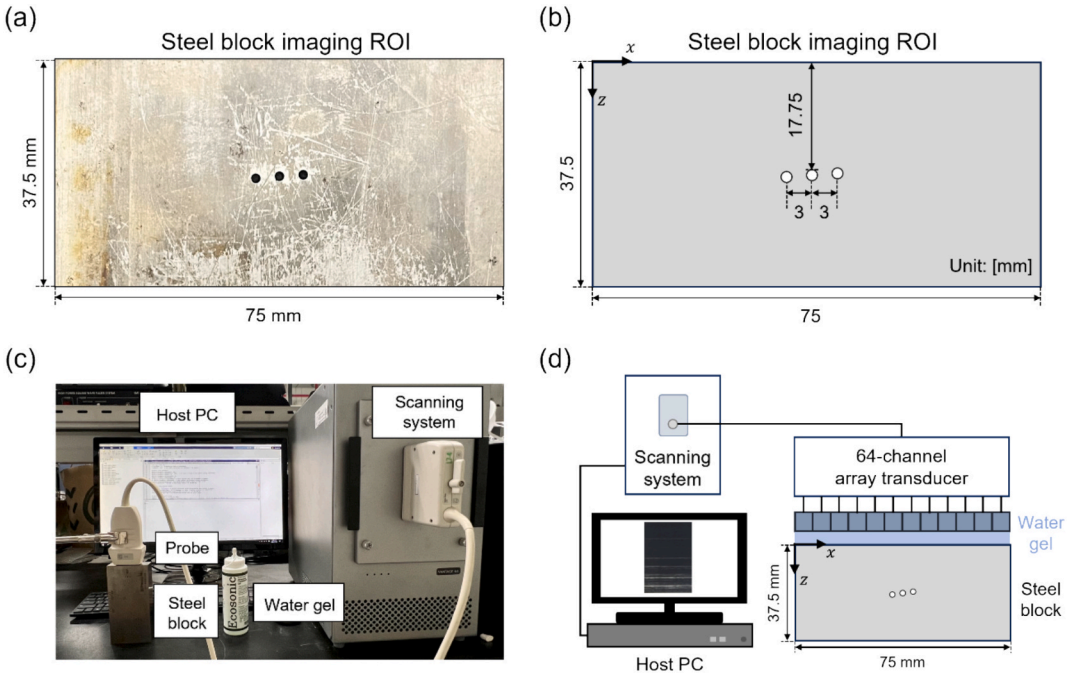

Fig. 7. Experimental setup for the steel sample: (a) photograph and (b) schematic of the steel block; and (c) photograph and (d) schematic of the ultrasonic imaging setup.

0.67 to 0.09, corresponding to a 64–98 % improvement compared with TFM. For FWHM, TFM-NSI outperforms the other beamformers, consistently producing narrower values. Even with only 8 elements, TFM-NSI achieves FWHM ranging from 0.43 to 0.01 mm, representing a substantial enhancement in spatial resolution. In comparison, TFM records an FWHM of 1.30 mm at 64 elements, marking a 67–99 % improvement in lateral resolution. The API values for the center hole, summarized in Table 3, demonstrate that TFM-NSI achieves reductions of 77 % to 93 % compared with TFM, confirming its ability to produce well-focused defect images with enhanced spatial resolution. In summary, the experimental results align closely with the simulation findings, confirming that TFM-NSI provides exceptional improvements in both resolution and contrast while effectively suppressing artifacts, even under sparse array conditions.

4.2. Application to other materials: NSI imaging for RC slab

To broaden the scope of the proposed NSI method, with particular emphasis on civil infrastructure systems, an RC slab with a longitudinal wave velocity (c_p = 3,578 m/s) was examined. In practice, ultrasonic imaging devices commonly used for monitoring internal structures are limited to 8–16 elements, which results in sparse array configurations and degraded image quality compared with methods used in other engineering fields. Based on the observations in this work, the NSI method stands out as a promising candidate for addressing the sparse array-induced limitation. To validate this, the sample was cast using the mix proportions and designed parameters summarized in Table 4. It was fabricated in accordance with the Korea Construction Specification (KCS) 14 20 00 for "Normal Concrete". Type I ordinary Portland cement (OPC), conforming to ASTM C150–22, was used as the binder, while river sand and crushed gravel, meeting ASTM C 33–18 requirements, served as fine and coarse aggregates, respectively. Chemical admixtures, including water reducers and air-entraining agents, were added to adjust the slump and air content of the fresh concrete mixture. As shown in Fig. 9, the RC slab had dimensions of 2,000 × 1,500 × 240 mm^3, with a designed compressive strength of

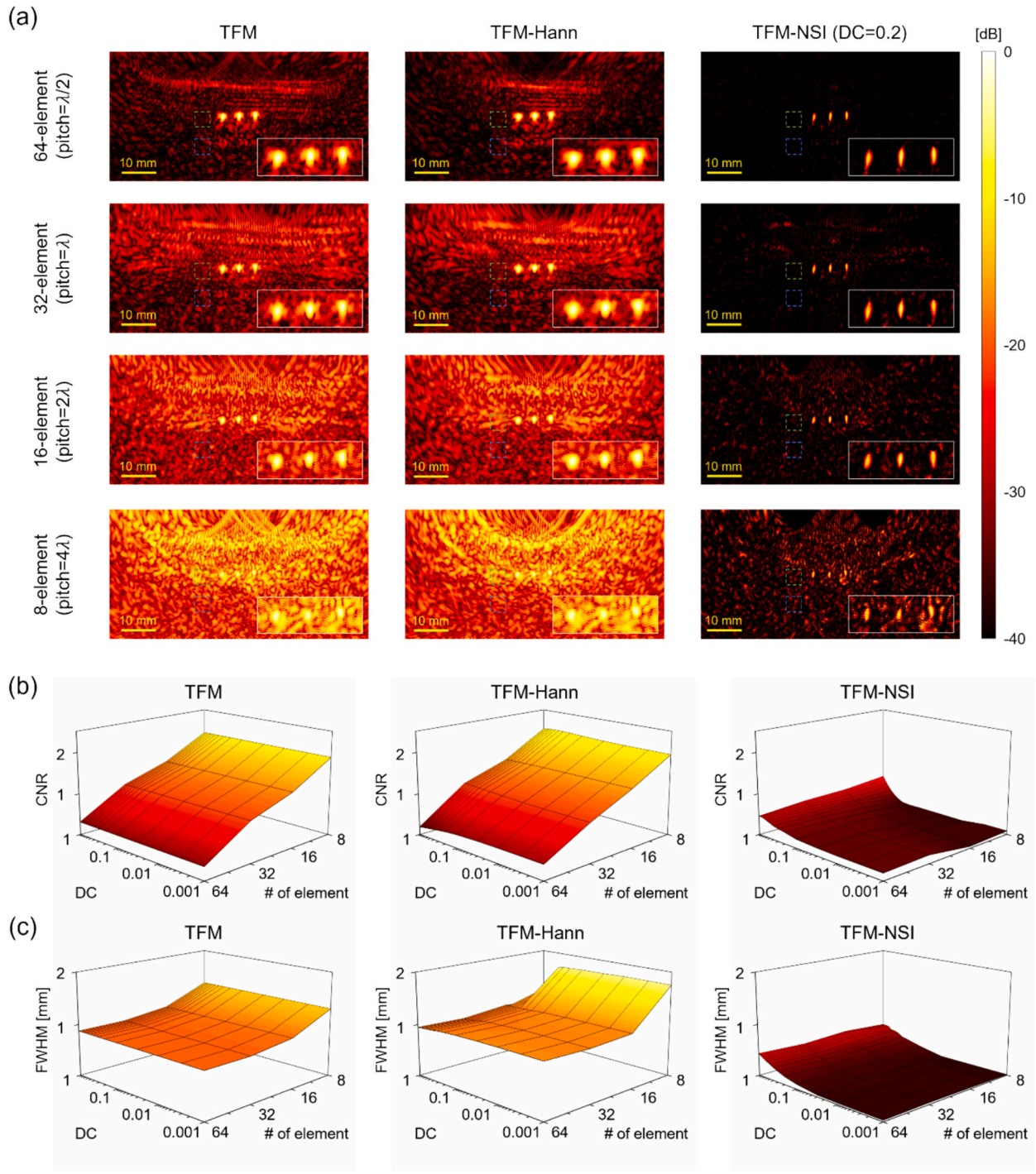

Fig. 8. Experimental results for the steel sample under varying levels of array sparsity: (a) reconstructed images using TFM, TFM-Hann, and TFM-NSI (DC = 0.2) beamformers, with green and blue boxes indicating the ROI and background noise regions for CNR measurement; (b) CNR matrix as a function of the number of elements and the DC constant; and (c) FWHM matrix as a function of the number of elements and the DC constant.

approximately 40 MPa. Rebars were embedded in a double-layer configuration, with horizontal spacing of 200 mm (x-direction) and 250 mm (y-direction), and vertical spacing of 70 mm (z-direction), as illustrated in the cross-sectional view in Fig. 9(c). To simulate internal damage, an artificial defect labeled D1 (Fig. 9(a)) was embedded in the slab to mimic delamination. Detailed information on the depth, shape, and size of the defect is provided in Table 5.

FMC data were collected using a Pundit 250 Array (Proceq, Switzerland) equipped with 8 elements and a pitch of 30 mm, as shown

Table 3
API values of each beamformer for the center hole: experimental results.

Number of elements	API		
	TFM	TFM-Hann	TFM-NSI (DC = 0.2)
64	0.58	0.67	0.04
32	0.59	0.66	0.05
16	0.62	0.66	0.14
8	0.74	0.69	0.15

Table 4
Mix proportion of concrete for slab.

W/C	Sand/gravel	Unit weight (kg/m^3)					Designed parameter		
		W	OPC (Type I)	Sand	Gravel	Chemical admixture	f_{ck} (MPa)	Slump (mm)	Air content (%)
0.33	43.3 %	170	517	745	995	6.75	40	150	3.5

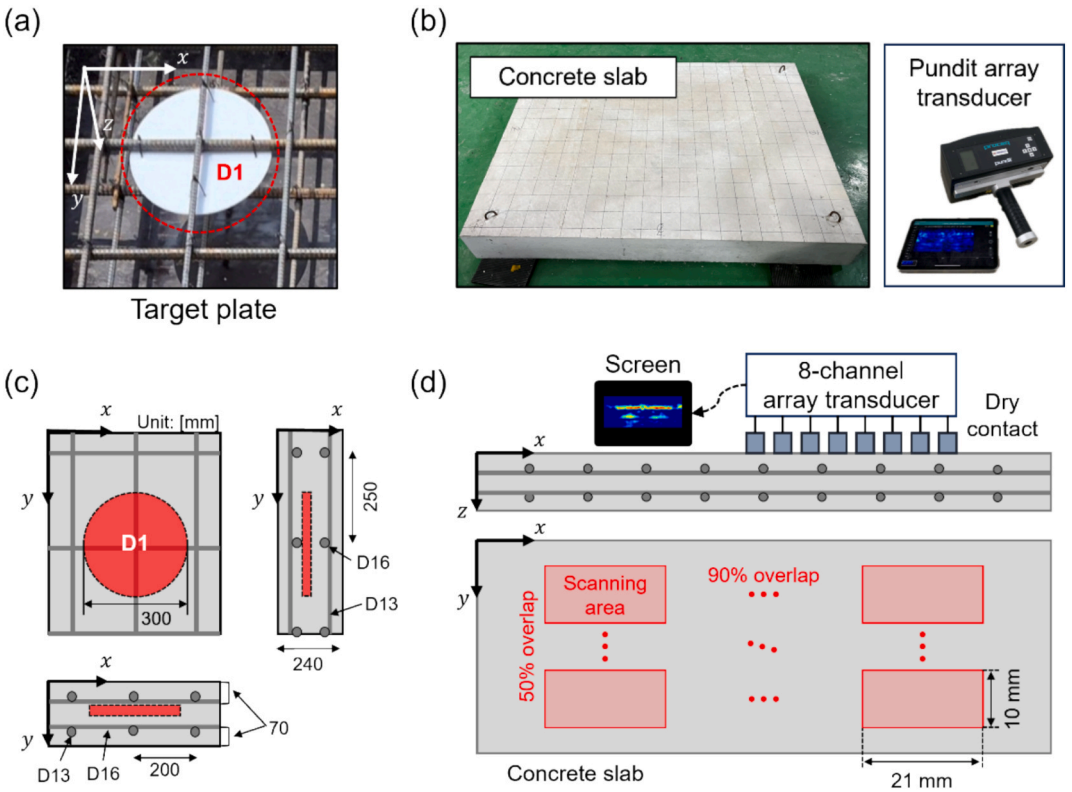

Fig. 9. Experimental setup and scanning configuration for RC slab imaging: (a) single artificial defect (D1) simulating delamination at the level of the top rebar layer; (b) the prepared RC slab (2,000 × 1,500 × 240 mm^3) with ultrasound array setup (8 elements, and 30 mm pitch); (c) cross-sectional geometry of the RC layers and delamination location; and (d) schematic of the ultrasound array setup and scanning area.

Table 5
Geometrical information of artificial defects embedded in the RC slab.

Defect type	Plate shape	Dimension [mm]	Location (depth) [mm]
Shallow delamination	Circle	300 (diameter)	99 (from surface)

in Figs. 9(b) and 9(d). To cover the entire slab surface, data acquisition was conducted at intervals of 20 mm in the x-direction and 50 mm in the y-direction. The collected data were then processed using the same TFM-NSI method to assess its effectiveness in RC structures. To achieve comprehensive visualization of the internal defect, 3D reconstruction was conducted using both the conventional TFM and the proposed TFM-NSI approach, as described in Fig. 10(a). During this process, 2D images were captured at 20 mm intervals along the x-direction and overlaid to form composite cross-sectional images. A total of 10 composite images were created, and spline interpolation was applied along the y-direction to ensure smooth data continuity. A comparative analysis was conducted with a

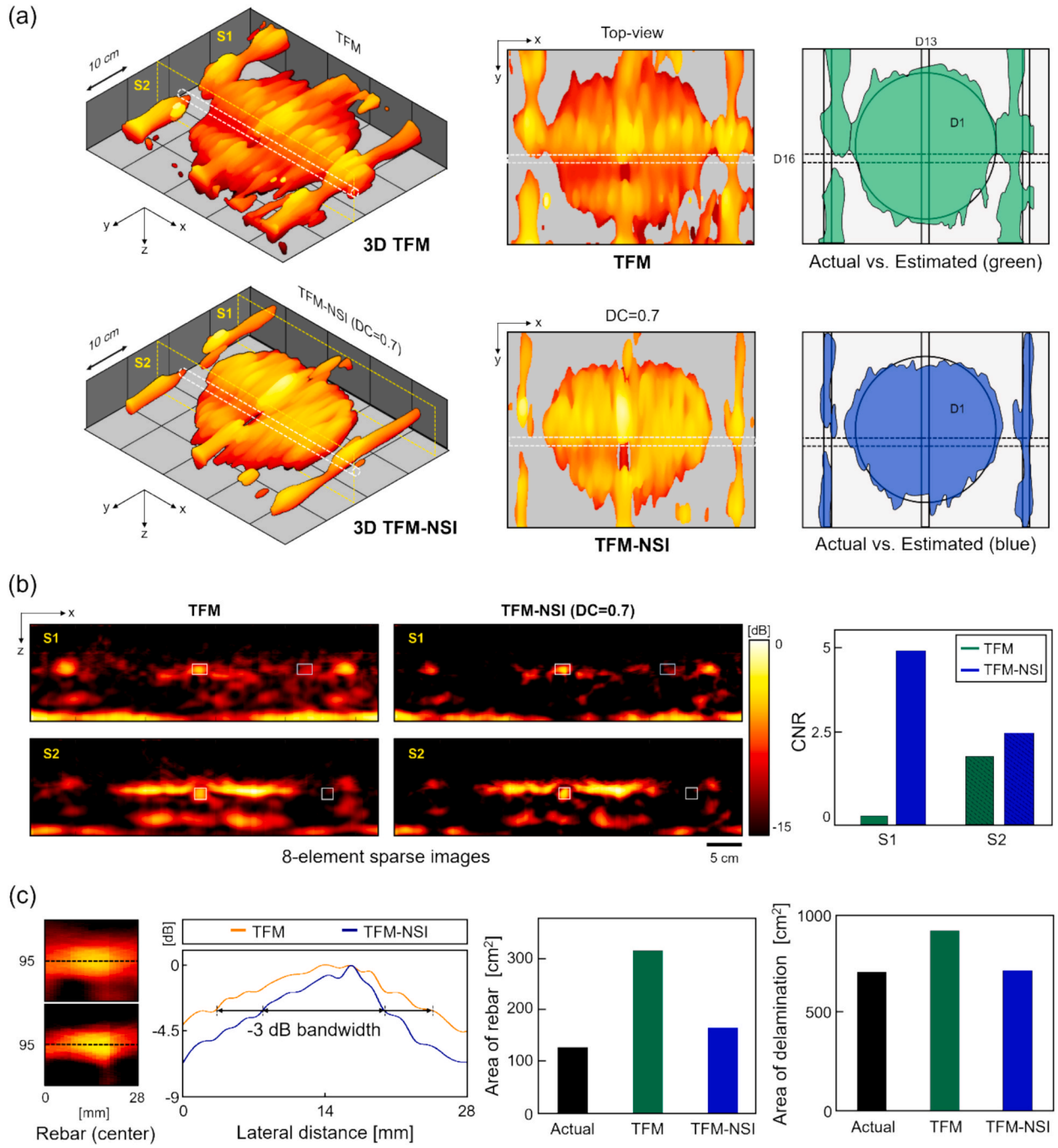

Fig. 10. Experimental result for RC slab: (a) 3D, top-view projection, and masked top-view images reconstructed using TFM and TFM-NSI (DC = 0.7); (b) cross-sectional images of TFM and TFM-NSI, with white boxes indicating the ROI and background noise regions used for CNR measurement; and (c) cross-sectional profiles of the rebar, along with the estimated areas of the rebar and delamination (derived from the masked top-view images in (a)).

DC constant of 0.7, focusing on ultrasound imaging data above −10 dB to enable a clear assessment of imaging performance (Fig. 10 (b)). The last two subfigures in Fig. 10(a) illustrate top-view 2D reconstructions overlaid with schematics of the actual defect, including rebar and delamination, with TFM contours in green and TFM-NSI contours in blue. In the 3D reconstruction, noticeable discontinuities in the rebar were observed due to the presence of transverse rebar. These discontinuities occur because rebar aligned along the x-axis is absent in 2D images taken along the same direction, resulting in interpolation artifacts in the final 3D reconstruction.

Fig. 10(c) provides a quantitative comparison of the projected area, enabling detailed assessment of accuracy for both methods. For the rebar, the actual area is 130 cm^2, while the TFM-NSI method produces a projection area of 168.7 cm^2 – a relatively small overestimation of 29.8 %. In contrast, the TFM method renders a significantly larger area of 320.5 cm^2, corresponding to an error of 146.5 %. Similarly, for the delamination area, the TFM-NSI method yields an estimated value of 715.1 cm^2, closely matching the actual value of 706.0 cm^2, with a discrepancy of only 1.3 %. In contrast, the TFM method produces an overestimated area of 918.8 cm^2, with an error of approximately 30.2 %. These findings verify that TFM-NSI provides a significantly closer representation of actual defects and internal features in RC structures.

Fig. 10(b) includes two representative 2D image slices, labeled as S1 and S2, obtained during the reconstruction process. These slices demonstrate significant improvements in CNR between the central rebar and non-defective regions when applying the TFM-NSI method. For the S1 image, TFM-NSI achieves a CNR of 4.88 compared to 0.24 for TFM, representing a 20-fold enhancement. In the S2 image, the CNR values are 2.57 for TFM-NSI and 1.91 for TFM, indicating a smaller but still 1.34-fold improvement. This relatively smaller difference in S2 is attributed to a higher standard deviation observed in the TFM-NSI region, which inflated the CNR denominator. A comparison of the FWHM values at −3 dB reveals that the TFM-NSI method achieves a narrower width of 11.1 mm, compared to 19.58 mm for TFM. These results are fully consistent with the simulation findings in Section 3.2, confirming that TFM-NSI provides high-resolution, high-contrast imaging while effectively suppressing artifacts in the lateral direction. The improvements in both CNR and FWHM further support the effectiveness of TFM-NSI for precisely detecting sub-rebar defects in RC structures. By delivering enhanced image clarity, particularly for defects with indistinct boundaries, the proposed TFM-NSI method demonstrates strong potential as a practical tool for internal structure assessments in complex, heterogeneous materials such as RC structures.

5. Conclusion

This study demonstrates the effectiveness of the proposed NSI technique in delivering high-quality ultrasound imaging of structural anomalies in solid engineering materials, including steel and RC structures. When integrated with the TFM beamformer, TFM-NSI significantly enhances contrast and lateral resolution, particularly in sparse array configurations. For steel structures, both numerical simulations and experimental results confirm that TFM-NSI effectively reduces the CNR of artifacts by suppressing side lobe and grating lobe levels. It also achieves narrower FWHM and lower API values for internal features (e.g., holes), resulting in sharp and well-focused defect images. These improvements become more pronounced with increased array sparsity: TFM-NSI with only 8 elements achieves image quality comparable to conventional TFM with 64 elements. Importantly, as an apodization-based method, TFM-NSI delivers these enhancements without increasing computational complexity, highlighting its effectiveness for field applications. Building on its validated performance in steel, TFM-NSI also applies effectively to RC structures. Experimental results confirm that it enables precise 3D visualization of rebar and internal defects while accurately measuring their dimensions. This advancement provides a new pathway toward timely, efficient, and reliable NDT for monitoring the internal condition of in-service concrete structures. Beyond its established use in biomedical imaging with dense arrays, this study validates that the proposed NSI beamformer can be effectively applied in other engineering domains, such as civil, mechanical, and material engineering, where sparse arrays are commonly accepted. It should be noted that TFM-NSI lacks improvement in vertical resolution since NSI is an apodization-based method that mainly affects the lateral beam pattern with limited influence in the vertical direction. Future work will explore enhancing vertical resolution through multiple NSI configurations located at different positions, as well as the development of new apodization functions for non-uniformly spaced arrays, to further broaden its applicability to diverse inspection conditions.

CRediT authorship contribution statement

Seungo Baek: Writing – original draft, Validation, Methodology, Investigation, Formal analysis. **Jinhee Kim:** Formal analysis. **Seohee Jeon:** Formal analysis. **Hyeong-Ki Kim:** Writing – review & editing, Validation, Resources. **Choon-Su Park:** Writing – review & editing, Supervision, Software, Resources. **Gun Kim:** Writing – review & editing, Supervision, Project administration, Funding acquisition, Conceptualization.

Declaration of competing interest

The authors declare that they have no known competing financial interests or personal relationships that could have appeared to influence the work reported in this paper.

Acknowledgments

The authors acknowledge funding support from Nanyang Technological University through the Tan Swan Beng Professorship in Construction Industry and the Start-up Grant (SUG) and the Ministry of Education, Singapore, under its Academic Research Fund Tier 1 Seed grant (RS33/24).

Appendix A. Numerical simulation with two closely spaced holes (0.75 λ and 0.25 λ): TFM vs. TFM-NSI

To further investigate improvements in lateral resolution, additional simulations are conducted with two closely spaced holes (spacings of 0.75 λ and 0.25 λ) under the same conditions described in Section 3.1. Fig. A1 presents the reconstructed images obtained with TFM and TFM-NSI (DC = 0.2), together with the corresponding lateral cross-sectional profiles plotted on a dB scale. When the holes are separated by 0.75 λ, the individual peaks produced by TFM begin to merge into a single peak, indicating that TFM cannot clearly resolve them (black line in Fig. A1(b)). In contrast, TFM-NSI still discerns the peaks at this spacing (red line in Fig. A1(b)). However, when the holes are placed closer at 0.25 λ, strong artifacts appear in the region between them for TFM-NSI. This trend is linked to an inherent limitation of DAS-based beamformers, resulting from the strong interference of point spread functions from adjacent objects. These results confirm that, in this study, the lateral resolution limit of TFM-NSI is approximately 0.25 λ.

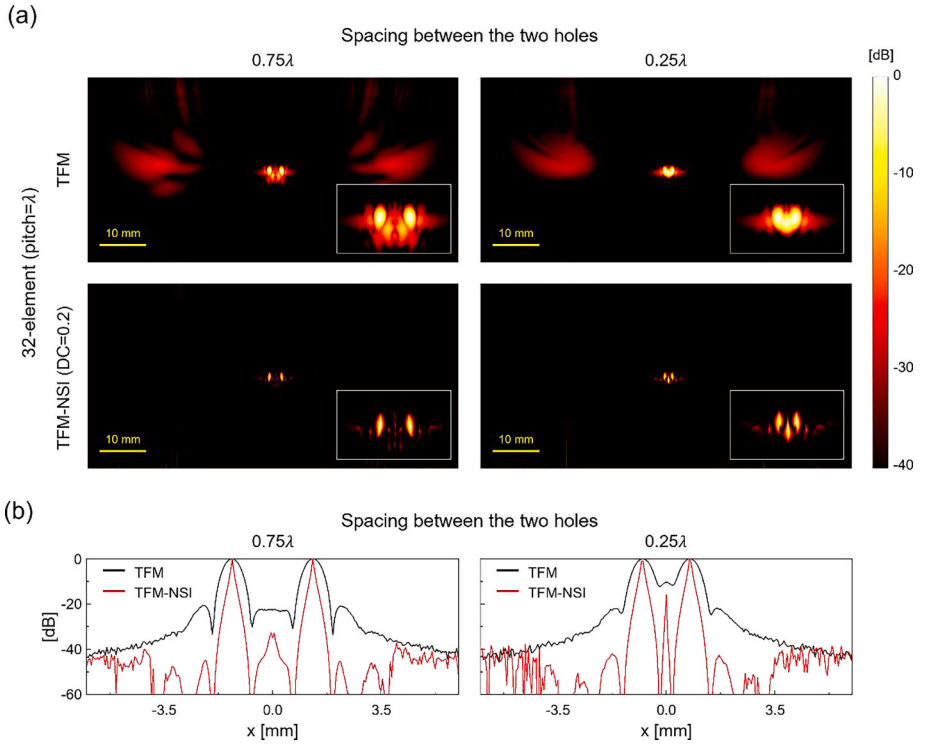

Fig. A1. Numerical simulation of two closely spaced holes at 0.75 and 0.25 spacing: (a) reconstructed images obtained using TFM and TFM-NSI (DC = 0.2) beamformers; and (b) the corresponding lateral cross-sectional profiles of the two holes (dB scale).

Data availability

Data will be made available on request.

References

[1] H.M. Jol, Ground Penetrating Radar Theory and Applications, Elsevier, 2008.
[2] T. Chen, G.Y. Tian, A. Sophian, P.W. Que, Feature extraction and selection for defect classification of pulsed eddy current NDT, NDT E Int. 41 (2008) 467–476, https://doi.org/10.1016/j.ndteint.2008.02.002.
[3] S. Zheng, J. Vanderstelt, J.R. McDermid, J.R. Kish, Non-destructive investigation of aluminum alloy hemmed joints using neutron radiography and X-ray computed tomography, NDT E Int. 91 (2017) 32–35, https://doi.org/10.1016/j.ndteint.2017.06.004.
[4] G. Kim, C.-W. In, J.-Y. Kim, K.E. Kurtis, L.J. Jacobs, Air-coupled detection of nonlinear Rayleigh surface waves in concrete—Application to microcracking detection, NDT E Int. 67 (2014) 64–70, https://doi.org/10.1016/j.ndteint.2014.07.004.
[5] G. Kim, J.-Y. Kim, K.E. Kurtis, L.J. Jacobs, Drying shrinkage in concrete assessed by nonlinear ultrasound, Cem. Concr. Res. 92 (2017) 16–20, https://doi.org/10.1016/j.cemconres.2016.11.010.
[6] G. Kim, G. Loreto, J.-Y. Kim, K.E. Kurtis, J.J. Wall, L.J. Jacobs, In situ nonlinear ultrasonic technique for monitoring microcracking in concrete subjected to creep and cyclic loading, Ultrasonics 88 (2018) 64–71, https://doi.org/10.1016/j.ultras.2018.03.006.
[7] S. Baek, H. Kim, G. Liyew, S. Park, J.H. Rhee, H.-K. Kim, G. Kim, On the inherent material states of ultra-high performance concrete from an acoustic perspective: linking mechanical properties to microstructural conditions, Constr. Build. Mater. 459 (2025) 139771, https://doi.org/10.1016/j.conbuildmat.2024.139771.
[8] S. Baek, K.Y. Kim, G. Kim, T.S. Yun, Linear and nonlinear ultrasound parameters attributed to anisotropy in granite, Sci. Rep. 14 (2024) 26986, https://doi.org/10.1038/s41598-024-78367-6.

[9] S. Baek, H.-K. Kim, M.L. Oelze, G. Kim, Can carbonation depth be measured in a nondestructive way? High-frequency quantitative ultrasound imaging for cement paste, Cem. Concr. Res. 180 (2024) 107519.
[10] W. Zhu, Y. Xiang, H. Zhang, M. Zhang, G. Fan, H. Zhang, Super-resolution ultrasonic Lamb wave imaging based on sign coherence factor and total focusing method, Mech. Syst. Signal Process. 190 (2023) 110121.
[11] C. Fan, S. Yu, Y. Zhao, Green function based ultrasonic super resolution imaging for defect location and characterization, Mech. Syst. Signal Process. 208 (2024) 110965, https://doi.org/10.1016/j.ymssp.2023.110965.
[12] E. Shaswary, J. Tavakkoli, J.C. Kumaradas, Efficient frequency-domain synthetic aperture focusing techniques for imaging with a high-frequency single-element focused transducer, IEEE Trans. Ultrason. Ferroelectr. Freq. Control 66 (2019) 57–70, https://doi.org/10.1109/TUFFC.2018.2881726.
[13] H. Jin, Z. Zheng, X. Liao, Y. Zheng, Image reconstruction of immersed ultrasonic testing for strongly attenuative materials, Mech. Syst. Signal Process. 168 (2022) 108654.
[14] G. Wang, C. Xu, Q. Lai, M. Deng, SAFT imaging for high-density polyethylene using quasi-static components of ultrasonic longitudinal waves, Ultrasonics 148 (2025) 107534, https://doi.org/10.1016/j.ultras.2024.107534.
[15] L. Chen, Z. Liu, Z. Zhang, Y. Zhu, X. Liu, J. Hu, C. He, Real-time imaging and geometric characterization of laser ultrasound based on array scanning optimization and delay-multiply-and-sum, Mech. Syst. Signal Process. 224 (2025) 112206, https://doi.org/10.1016/j.ymssp.2024.112206.
[16] D. Chen, H. Xiao, J. Xu, An improved Richardson-Lucy iterative algorithm for C-scan image restoration and inclusion size measurement, Ultrasonics 91 (2019) 103–113.
[17] C. Dalitz, R. Pohle-Frohlich, T. Michalk, Point spread functions and deconvolution of ultrasonic images, IEEE Trans. Ultrason. Ferroelectr. Freq. Control 62 (2015) 531–544.
[18] K.-N. Ying, C.-Y. Ni, L.-N. Dai, W.-X. Cao, Z. Yang, W.-W. Kan, L. Yuan, Z.-H. Shen, Image quality improvement in multi-mode laser ultrasound imaging using reconstructed synthetic aperture focusing technique, Struct. Heal. Monit. (2024), 14759217231221316.
[19] R. Ludwig, D. Roberti, A nondestructive ultrasonic imaging system for detection of flaws in metal blocks, IEEE Trans. Instrum. Meas. 38 (1989) 113–118.
[20] M. Schickert, Progress in ultrasonic imaging of concrete, Mater. Struct. 38 (2005) 807–815.
[21] B.W. Drinkwater, P.D. Wilcox, Ultrasonic arrays for non-destructive evaluation: a review, NDT E Int. 39 (2006) 525–541, https://doi.org/10.1016/j.ndteint.2006.03.006.
[22] B. Diarra, H. Liebgott, M. Robini, P. Tortoli, C. Cachard, Optimized 2D array design for Ultrasound imaging, in: 2012 Proc. 20th Eur. Signal Process. Conf., IEEE, 2012: pp. 2718–2722.
[23] D.H. Turnbull, F.S. Foster, Fabrication and characterization of transducer elements in two-dimensional arrays for medical ultrasound imaging, IEEE Trans. Ultrason. Ferroelectr. Freq. Control 39 (1992) 464–475.
[24] B.D. Steinberg, Principles of aperture and array system design: including random and adaptive arrays, N. Y. (1976).
[25] O. Martínez-Graullera, C.J. Martín, G. Godoy, L.G. Ullate, 2D array design based on Fermat spiral for ultrasound imaging, Ultrasonics 50 (2010) 280–289, https://doi.org/10.1016/j.ultras.2009.09.010.
[26] M. Karaman, I.O. Wygant, Ö. Oralkan, B.T. Khuri-Yakub, Minimally redundant 2-D array designs for 3-D medical ultrasound imaging, IEEE Trans. Med. Imaging 28 (2009) 1051–1061.
[27] L. Moreau, B.W. Drinkwater, P.D. Wilcox, Ultrasonic imaging algorithms with limited transmission cycles for rapid nondestructive evaluation, IEEE Trans. Ultrason. Ferroelectr. Freq. Control 56 (2009) 1932–1944.
[28] H. Hu, J. Du, N. Xu, H. Jeong, X. Wang, Ultrasonic sparse-TFM imaging for a two-layer medium using genetic algorithm optimization and effective aperture correction, NDT E Int. 90 (2017) 24–32.
[29] H. Peng, J. Peng, H. Zhu, Z. Wang, X. Gao, The efficiency optimization of full matrix capture imaging detection based on increasing the effective aperture, in: 2014 IEEE Far East Forum Nondestruct. Eval., IEEE, 2014: pp. 50–56.
[30] C. Holmes, B.W. Drinkwater, P.D. Wilcox, Post-processing of the full matrix of ultrasonic transmit–receive array data for non-destructive evaluation, NDT E Int. 38 (2005) 701–711, https://doi.org/10.1016/j.ndteint.2005.04.002.
[31] C. Holmes, B.W. Drinkwater, P.D. Wilcox, Advanced post-processing for scanned ultrasonic arrays: Application to defect detection and classification in non-destructive evaluation, Ultrasonics 48 (2008) 636–642, https://doi.org/10.1016/j.ultras.2008.07.019.
[32] J. Li, S. Wang, X. Mao, W. Liu, H. Wang, S. Zhou, Accelerating algorithm for total focusing method imaging based on optimization of full matrix data, Russ. J. Nondestruct. Test. 59 (2023) 161–170, https://doi.org/10.1134/S1061830922600642.
[33] M. Chen, C. Weng, X. Xu, K. Yang, D. Mei, J. Chen, H. Jin, 3D ultrasonic full matrix capture imaging for cylindrical scans with wavenumber-domain reconstruction, Mech. Syst. Signal Process. 217 (2024) 111528.
[34] F.J. Harris, On the use of windows for harmonic analysis with the discrete Fourier transform, Proc. IEEE 66 (1978) 51–83.
[35] T. de A. Prado, H.L. Moura, T.A.R. Passarin, G.A. Guarneri, G.P. Pires, D.R. Pipa, A straightforward method to evaluate the directivity function of ultrasound imaging systems, NDT E Int. 119 (2021) 102402.
[36] D. Teng, L. Liu, Y. Xiang, F.-Z. Xuan, An optimized total focusing method based on delay-multiply-and-sum for nondestructive testing, Ultrasonics 128 (2023) 106881.
[37] J. Camacho, M. Parrilla, C. Fritsch, Phase coherence imaging, IEEE Trans. Ultrason. Ferroelectr. Freq. Control 56 (2009) 958–974.
[38] J. Camacho, C. Fritsch, Phase coherence imaging of grained materials, IEEE Trans. Ultrason. Ferroelectr. Freq. Control 58 (2011) 1006–1015.
[39] R. Schmidt, Multiple emitter location and signal parameter estimation, IEEE Trans. Antennas Propag. 34 (1986) 276–280.
[40] S. Sternini, A. Pau, F.L. Di Scalea, Minimum-variance imaging in plates using guided-wave-mode beamforming, IEEE Trans. Ultrason. Ferroelectr. Freq. Control 66 (2019) 1906–1919.
[41] H. Masoom, R.S. Adve, R.S.C. Cobbold, Target detection in diagnostic ultrasound: Evaluation of a method based on the CLEAN algorithm, Ultrasonics 53 (2013) 335–344, https://doi.org/10.1016/j.ultras.2012.06.016.
[42] A. Gholampour, S.M. Sakhaei, S.M.H. Andargoli, A robust approach to apodization design in phased arrays for ultrasound imaging, Ultrasonics 76 (2017) 10–18, https://doi.org/10.1016/j.ultras.2016.12.009.
[43] C.H. Seo, J.T. Yen, Sidelobe suppression in ultrasound imaging using dual apodization with cross-correlation, IEEE Trans. Ultrason. Ferroelectr. Freq. Control 55 (2008) 2198–2210.
[44] S. Majhi, A. Mukherjee, A. Ganguli, Enhanced ultrasonic imaging in concrete structures with spatial apodization filters, J. Mater. Civ. Eng. 33 (2021) 4021266.
[45] Y. Shen, P. Wang, L. Tong, J. Chen, Q. Li, J. Zhu, K. Wang, J. Zeng, A low-complexity beamformer for ultrasound imaging based on sub-beamformer and multi-apodization with cross-correlation, Ultrasound Med. Biol. 50 (2024) 1551–1565, https://doi.org/10.1016/j.ultrasmedbio.2024.06.011.
[46] H.C. Stankwitz, R.J. Dallaire, J.R. Fienup, Nonlinear apodization for sidelobe control in SAR imagery, IEEE Trans. Aerosp. Electron. Syst. 31 (1995) 267–279.
[47] C.H. Seo, J.T. Yen, Evaluating the robustness of dual apodization with cross-correlation, IEEE Trans. Ultrason. Ferroelectr. Freq. Control 56 (2009) 291–303.
[48] A.S. Savoia, G. Caliano, G. Matrone, G. Magenes, A. Ramalli, E. Boni, P. Tortoli, Improved lateral resolution and contrast in ultrasound imaging using a sidelobe masking technique, in: 2014 IEEE Int. Ultrason. Symp., IEEE, 2014: pp. 1682–1685.
[49] A. Agarwal, J. Reeg, A.S. Podkowa, M.L. Oelze, Improving spatial resolution using incoherent subtraction of receive beams having different apodizations, IEEE Trans. Ultrason. Ferroelectr. Freq. Control 66 (2019) 5–17, https://doi.org/10.1109/TUFFC.2018.2876285.
[50] M. Gardner, R.J. Miller, M.L. Oelze, Grating lobe mitigation on large-pitch arrays using null subtraction imaging, Ultrasonics 140 (2024) 107302, https://doi.org/10.1016/j.ultras.2024.107302.
[51] Z. Kou, R.J. Miller, M.L. Oelze, Grating lobe reduction in plane-wave imaging with angular compounding using subtraction of coherent signals, IEEE Trans. Ultrason. Ferroelectr. Freq. Control 69 (2022) 3308–3316.
[52] Z. Kou, M.R. Lowerison, Q. You, Y. Wang, P. Song, M.L. Oelze, High-resolution power doppler using null subtraction imaging, IEEE Trans. Med. Imaging 43 (2024) 3060–3071, https://doi.org/10.1109/TMI.2024.3383768.

[53] M. Yociss, K. Brown, K. Hoyt, Null Subtraction Beamforming for Improved Vessel Resolution in Volumetric Contrast-Enhanced Ultrasound, in: 2021 IEEE Int. Ultrason. Symp., 2021: pp. 1–4. doi:10.1109/IUS52206.2021.9593368.
[54] V. Perrot, M. Polichetti, F. Varray, D. Garcia, So you think you can DAS? a viewpoint on delay-and-sum beamforming, Ultrasonics 111 (2021) 106309.
[55] S. Baek, G. Kim, J.-Y. Kim, Nonlinear standing waves for assessing material nonlinearity in thin samples, Ultrasonics 142 (2024) 107385, https://doi.org/10.1016/j.ultras.2024.107385.
[56] B.E. Treeby, J. Jaros, D. Rohrbach, B.T. Cox, Modelling elastic wave propagation using the k-wave matlab toolbox, in: 2014 IEEE Int. Ultrason. Symp., IEEE, 2014: pp. 146–149.